CuO-CeO_2 nanocomposite catalysts produced by mechanochemical synthesis

Cite as: AIP Advances **9**, 065115 (2019); https://doi.org/10.1063/1.5109067
Submitted: 06 May 2019 . Accepted: 11 June 2019 . Published Online: 25 June 2019

Ch. Borchers, M. L. Martin, G. A. Vorobjeva, O. S. Morozova, A. A. Firsova, A. V. Leonov, E. Z. Kurmaev, A. I. Kukharenko, I. S. Zhidkov, and S. O. Cholakh

CuO-CeO_2 nanocomposite catalysts produced by mechanochemical synthesis

Cite as: AIP Advances 9, 065115 (2019); doi: 10.1063/1.5109067
Submitted: 6 May 2019 • Accepted: 11 June 2019 •
Published Online: 25 June 2019

Ch. Borchers,[1,a)] M. L. Martin,[1] G. A. Vorobjeva,[2] O. S. Morozova,[2] A. A. Firsova,[2] A. V. Leonov,[3] E. Z. Kurmaev,[4,5] A. I. Kukharenko,[4,5] I. S. Zhidkov,[5] and S. O. Cholakh[5]

AFFILIATIONS

[1]Institute for Materials Physics, University of Göttingen, Friedrich-Hund-Platz 1, D-37077 Göttingen, Germany
[2]Semenov Institute of Chemical Physics RAS, Kosygin st. 4, 119991 Moscow, Russia
[3]Lomonosov Moscow State University, Chemical Department, Leninskie Gory, 119899 Moscow, Russia
[4]M.N. Mikheev Institute of Metal Physics, RAS-Ural Division, Kovalevskaya Str. 18, 620108 Yekaterinburg, Russia
[5]Institute of Physics and Technology, Ural State University, Mira Str. 19, 620002 Yekaterinburg, Russia

[a)]**Corresponding author e-mail:** chris@ump.gwdg.de

ABSTRACT

Mechanochemical synthesis based on ball-milling of individual oxides was applied as a one-step preparation technique for CuO-CeO_2 catalyst for preferential CO oxidation in H_2 excess. The mechanical energy dose transferred to the original powder mixture determines both the catalyst composition and activity. It is found that after 90 min of milling (corresponding to a dose of 372 kJ mol^{-1}), a mixture of 10 wt.% CuO-CeO_2 powder exhibits a CO conversion of 97% at 423 K. Four active oxygen states, which are not observed in case of pure CeO_2, were detected in the nanocomposite lattice and attributed to the presence of Cu in surface sites as well as in subsurface bulk sites of CeO_2, in nearest neighbor and next nearest neighbor positions. Correspondingly, oxidation of CO to CO_2 was found to occur in a two-stage process with T_{max} = 395/460 K, and oxidation of H_2 to H_2O likewise in a four-stage process with T_{max} = 426/448/468/516 K. The milled powder consists of CeO_2 crystallites sized 8–10 nm agglomerated to somewhat larger aggregates, with CuO dispersed on the surface of the CeO_2 crystallites, and to a lesser extent present as Cu_2O.

I. INTRODUCTION

CuO-CeO_2 catalysts are widely used in commercially and ecologically important processes, especially in CO-preferential oxidation (CO-PROX) - low temperature oxidation of CO in excess hydrogen (Li et al., 2010; Maciel et al., 2011; Martínez-Arias et al., 2013; Wongkaew et al., 2013; Galvita et al., 2014; Monte et al., 2014; Yao et al., 2014; Ding et al., 2018; Hossain et al., 2018; Jing et al., 2019; and Zhao et al., 2019). Cu successfully substitutes for platinum group and gold group metals (Me) in Me-CeO_2 systems (Avgouropoulos et al., 2002; Shapovalov and Metiu, 2007; Kim et al., 2008; and Liu and Corma, 2018). CeO_2 is a promoter of CO-PROX reaction due to its easy reducibility, high oxygen storage capability, and high oxygen mobility. The latter is stimulated by formation of surface and lattice point defects, induced by Cu incorporated into the CeO_2 surface (Vanpoucke et al., 2014; Elias et al., 2016). Thus, the synergetic interaction between CuO and CeO_2 is the major factor in the catalytic activity and selectivity of this system. The active sites for CO oxidation are located at interfaces between both oxides, as follows from detailed studies of CuO-CeO_2 and inverse CeO_2-CuO supported catalysts (Senanayake et al., 2013; Zeng et al., 2013). X-ray photoelectron spectroscopy (XPS) measurements show the appearance of a new oxygen state different from that in CuO and CeO_2, which is attributed to low-coordinated oxygen located near surface or subsurface defects or oxygen in the surface hydroxyl groups (Tang et al., 2005; Kydd et al., 2009; Borchers et al., 2016; Song et al., 2016; and Ren et al., 2017). Synergy in CuO and CeO_2 redox properties is proven by temperature programmed

reduction (TPR) experiments confirming a significant decrease in the reduction temperature, as compared to individual oxides (Ren et al., 2017; Liu and Flytzani-Stephanopoulos, 1996; Qi and Flytzani-Stephanopoulos, 2004; and Polster et al., 2009). Both are indicative of a new CuO-CeO_2 composition being formed: CuO nanoinclusions in CeO_2 or $Cu_xCe_{1-x}O_y$ solid solutions. However, the real nature of these active structures (solid solution, lattice defects, surface clusters, etc.) is still under discussion. According to results found in literature, the best catalyst composition contains approximately 5 wt.% CuO in CeO_2 (Il'ichev et al., 2006; Luo et al., 2007). All catalyst preparation techniques are concentrated on designing nanomaterials with enlarged CuO-CeO_2 interfaces. Correspondingly, catalytic properties observed in catalysts prepared by different techniques are very similar. The most commonly used techniques are wet impregnation, co-precipitation, sol-gel method, urea-nitrate combustion and hydrothermal methods (Yang et al., 2009; Prasad and Rattan, 2010 and references therein; Maciel et al., 2012; and Cecilia et al., 2017).

In this work, mechanochemical synthesis by ball-milling is applied to prepare CuO-CeO_2 systems containing 10 wt.% CuO and 90 wt.% CeO_2 from individual oxides. Two major processes are realized under the ball milling: powder intermixing and severe plastic deformation. The collisions with the balls result in high local surface pressures up to 10 – 20 GPa (Streletskii, 1991), concurrent powder intermixing leads to nanocomposite materials with high concentrations of structural defects and enlarged interfaces between the components. This method is carried out rapidly, is of low cost, and ecologically friendly. With the use of mechanochemical synthesis we obtained a series of CuO-CeO_2 composites, the structural, morphological, redox and catalytic properties of which were studied in dependence of the milling conditions. The samples were tested in CO-PROX reaction and characterized by Brunauer-Emmett-Teller (BET) adsorption isotherms, X-ray diffraction (XRD), high resolution transmission electron microscopy (HRTEM), X-ray photoelectron spectroscopy (XPS), and temperature-programmed reduction (TPR) measurements. A constant concentration of CuO in CeO_2 was chosen in order to focus on the effect of milling conditions on the catalyst.

II. METHODS

10 wt.% CuO-CeO_2 powders were prepared by ball-milling of CuO and CeO_2 powders with specific surface areas $S < 1$ m^2 g^{-1} and $S = 89$ m^2 g^{-1}, respectively. Oxides were obtained by decomposition of $Cu(NO_3)_2{\cdot}2.5H_2O$ and $Ce(NO_3)_3{\cdot}6H_2O$ (both of 99% purity, Aldrich) in air by heating with a rate of 7 K min^{-1} up to 773 K and subsequently calcinating at this temperature for two hours. Before milling, copper oxide and ceria powders were mixed in an agate mortar. Ball-milling was carried out in air at room temperature under static conditions in a mechanochemical reactor fixed to the vibrator. A stainless steel container was loaded with 1.8 g of CuO-CeO_2 reaction mixture, consisting of 0.18 g of CuO and 1.62 g of CeO_2, together with 15.3 g of hardened steel balls with diameter 3 – 5 mm; the vibration frequency was 50 Hz with an amplitude of 7.25 mm; the average energy intensity was 0.8 W/g. The powder was milled for 30, 60, 90 and 120 min, corresponding to energy doses of 124, 248, 372 and 496 kJ mol^{-1}, respectively (CuO: 79.545 g mol^{-1}; CeO_2: 172.115 g mol^{-1}).

The specific surface area S was measured by the Brunauer-Emmett-Teller (BET) method using low-temperature Ar adsorption. Chemical analysis was performed by atomic absorption spectroscopy (AAS) with a ThermoScientific iCAP 6300 Duo. The bulk composition after different stages of treatment (original, as milled, as reduced and as-used in CO-PROX) was studied by X-ray diffraction (XRD) using a Dron-3 diffractometer with Cu-Kα radiation. The powder phase composition was determined using JCPDS files provided by the International Center for Diffraction Data. Quantitative X-ray phase analysis was performed with a fitting procedure, where the experimental spectra were approximated with a linear combination of the theoretical spectra of phases and the background using optimized values of lattice parameters and parameters of broadening of the diffraction maxima of phases (Shelekhov and Sviridova, 2000). Crystallite sizes were calculated using the Scherrer equation (Scherrer, 1918) and according to Shelekhov and Sviridova, (2000) in the case of CeO_2.

Microstructure and morphology were studied by scanning (SEM), transmission electron microscopy (TEM), and high resolution transmission electron microscopy (HRTEM). SEM micrographs were obtained with a Philips SEM 515. TEM and HRTEM investigations were carried out on a Philips CM 200 UT electron microscope operated at an accelerating voltage of 200 kV equipped with an energy dispersive X-ray spectroscopy (EDS) system. Powdered sample particles were distributed on 3mm gold grids covered by an amorphous carbon film.

The surface composition, chemical and electronic state of Ce, Cu and O atoms were investigated by X-ray photoelectron spectroscopy (XPS). XPS spectra were recorded with a PHI 5000 VersaProbe electron spectrometer (ULVAC-Physical Electronics, USA) using 25 W Al-Kα radiation. The samples were placed in the forechamber of the system, which was pumped down to 10^{-7} Pa and held under vacuum for 24 h to minimize the influence of oxygen from the atmosphere. XPS spectra of reference samples CuO, Cu_2O, Ce_2O_3 and CeO_2 were measured under the same conditions. Binding energies were referenced to the C *1s* line at 285 eV from adventitious carbon and identified using the ULVAC-PHI MULTIPAK program.

Temperature-programmed reduction experiments (H_2-TPR and CO-TPR, respectively) for original and as-milled powders were carried out under conditions of differential scanning calorimetric analysis (DSC) and thermogravimetric analysis (TG) on a simultaneous TG-DTA/DSC apparatus (NETZSCH STA 449C, Germany) equipped with a mass-spectrometer (MS) AEOLOS-32 in a temperature range of 323 – 673 K with a heating rate of 10 K/min. Samples of 15 mg were loaded and dried in He flow under temperature programming conditions from 293 to 473 K. After the samples were cooled to 293 K and pumped 3 – 4 times, a reduction agent consisting of 10 vol.% H_2/Ar-He or 10 vol.% CO/Ar-He was introduced with a flow rate of 80 ml/min; for experiments like these, 10% of active agent in inert gas is typical, see, e.g. Zeng et al. (2013), He acts as carrier gas in the setup. All gases were of 99.999% purity.

The catalytic activity was tested in the temperature range of 323 – 673 K without pre-treatment. A flow set-up was equipped with a quartz reactor (tube diameter 3 mm) combined with a gas-preparation system and a gas-chromatograph with a thermal-conductivity detector and analytic columns (NaX(13A) and

Porapak QS). The reactor was charged with 20 mg of the catalyst; the reaction mixture (98 vol.% H_2, 1 vol.% CO and 1 vol.% O_2) was blown through the reactor with a flow rate of 40 ml min^{-1}.

III. RESULTS

A. Microstructure, morphology, and reducibility of starting CuO and CeO_2

Figure 1 shows SEM micrographs and an XRD spectrum of the CuO powder. It consists of the monoclinic tenorite (JCPDS 5-661). The original powder exhibits rounded agglomerates consisting of plate-like particles 1 – 3 μm in diameter and about 0.1 μm thick, shown in Fig. 1a). The original powder is very brittle and its morphology has completely changed after 60 min of milling: a fine powder with agglomerates consisting of flat clustered particles is obtained, see Fig. 1b). Figure 1c) shows XRD patterns of CuO original (spectrum 1) and milled for 60 min (spectrum 2). Significant XRD peak broadening suggests remarkable crystallite size reduction from about 30 to about 5 nm, and a high concentration of structural defects. The CeO_2 powder is shown in Fig. 2: it adopts a fluorite-type fcc structure with lattice constant a = 541.1 pm. The powder particles are non-uniform in size and in shape: rather large particles coexist with much smaller ones, see Fig. 2a). Smaller particles are often lumped together on the surfaces of large particles. The powder becomes more uniform and more compact after 60 min of milling, see Fig. 2b). However, an insignificant change in XRD peak broadening is observed, see Fig. 2c). The crystallite size remains virtually unchanged at about 10 – 12 nm.

Figure 3a) shows TG curves recorded for CuO reduction under H_2-TPR conditions, and Fig. 3b) shows TG curves corresponding to CO-TPR of original and as-milled CuO powders. The morphological changes affected the kinetics of CuO reducibility: the processes in both H_2 and CO are carried out faster and at remarkably lower temperatures. As can be seen, 50% of CuO transformation to Cu is realized at 552 K in case of as-milled and instead of 694 K for original powders (CuO contains ~20 wt.% of oxygen; the mass loss from 100% to 90% is 10% - half of the oxygen is taken away). The powder originally consisting of unmilled CuO still contains about 22 wt.% CuO, 68 wt.% Cu_2O, and 10 wt.% Cu after heating to 673 K. The CuO powder milled for 60 min contains about 8 wt.% CuO, 69 wt.% Cu_2O, and 23 wt.% Cu, according to quantitative XRD analysis. No reduction of CeO_2 original and as-milled was observed during H_2-TPR. This is likely due to the absence of surface sites suitable for H_2 dissociative chemisorption. Figure 3c) shows TG curves corresponding to CO-TPR of original and as-milled CeO_2 powders. As-milled CeO_2 reduces faster than as-received powder in spite of a remarkable decrease in specific surface area from about 90 to about 46 m^2 g^{-1}. In terms of figures, $CeO_{1.99}$ and $CeO_{1.98}$ are formed after CO-TPR from original and as-milled ceria powders, respectively; the calculation revealed that only a small part of the surface oxygen participates in the process. In terms of surface single layer of one CeO_2 unit cell thickness (541.1 pm), it was about 10% and 25% for CeO_2 original and milled, respectively. Thus, instead of bulk reduction observed for CuO samples, only partial surface reduction of CeO_2 is carried out under the same CO-TPR conditions.

Fig. 4 shows the temperature dependence of MS peak intensity (m/e = 44, CO_2) for original CuO and CeO_2 powders, respectively.

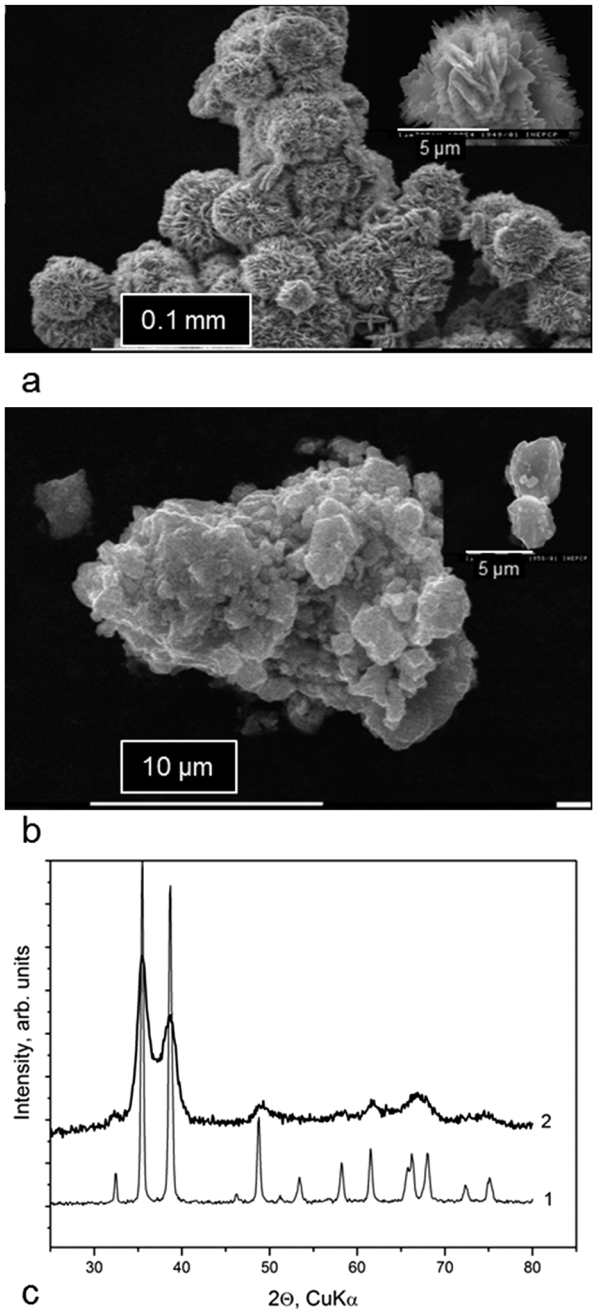

FIG. 1. SEM images of a) original CuO powder containing rounded agglomerates consisting of plate-like particles 1–3 μm in diameter and about 0.1 μm thick and b) CuO powder milled for 60-min containing a fine particles with agglomerates consisting of flat clustered particles. c) The XRD patterns of (1) CuO original and (2) milled for 60 min.

The most important fact is that the two-stage CuO reduction (the first stage is CuO to Cu_2O reduction, the next stage is the final transformation of Cu_2O to Cu) is described in TPR by single peak profiles in the temperature range of 323 – 673 K. It means that

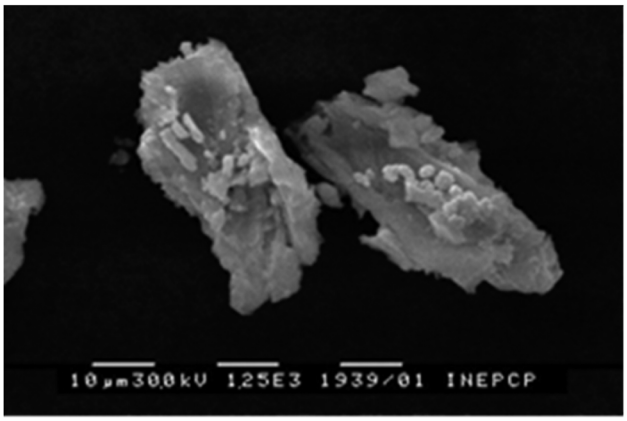

a

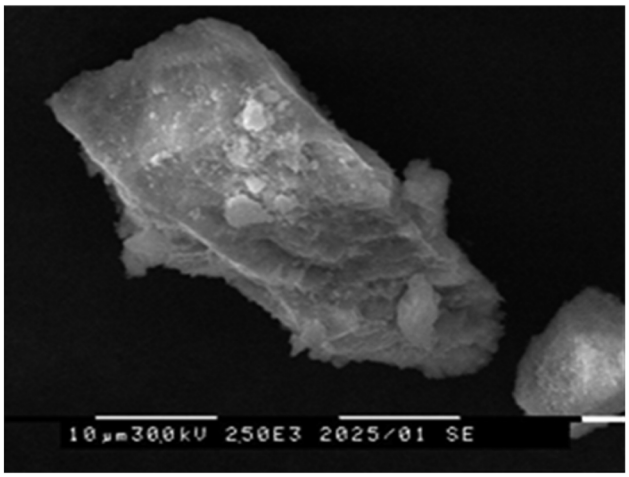

b

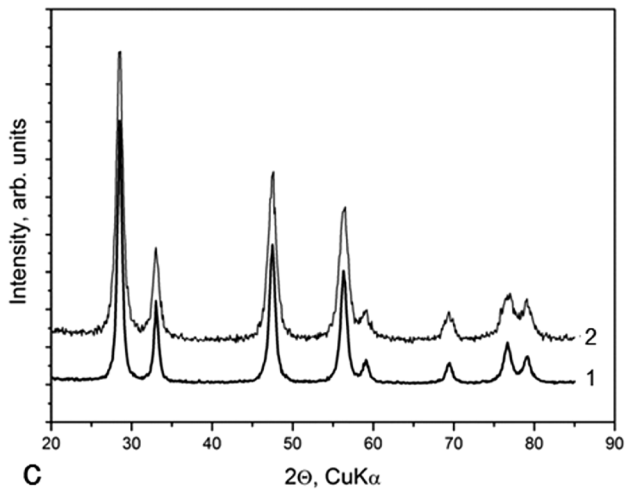

c

FIG. 2. SEM images of a) original CeO_2 powder containing non-uniform in size and in shape particles: rather large particles coexist with much smaller ones and b) CeO_2 powder after 60 min of milling containing more uniform and more compact particles. c) The XRD patterns of (1) CeO_2 original and (2) milled for 60 min.

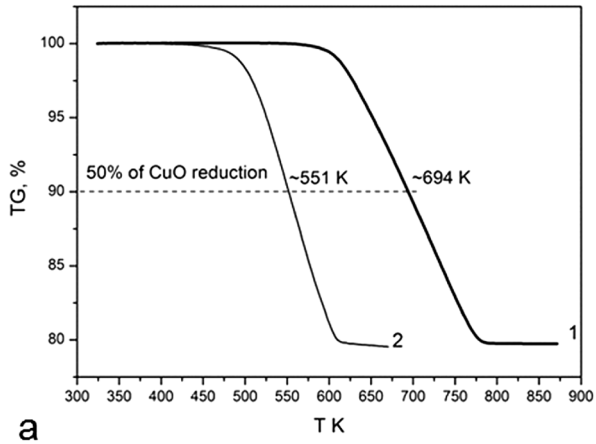

a

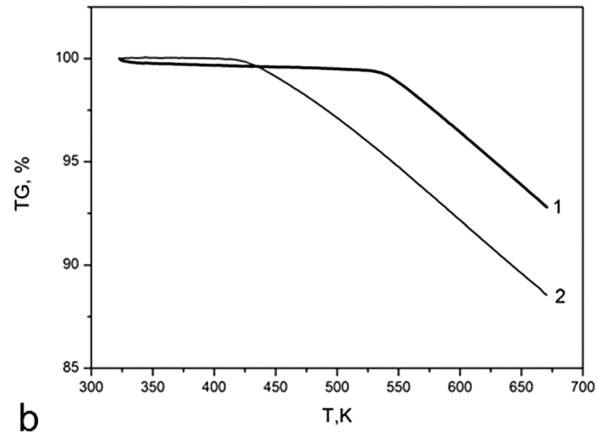

b

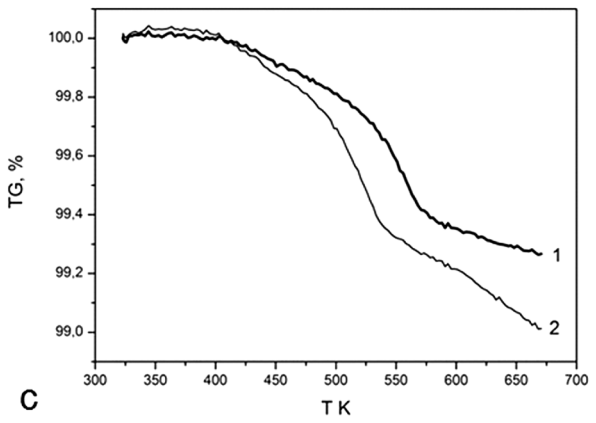

c

FIG. 3. TG curves for a) CuO reduction under H2-TPR and b) CO-TPR for (1) CuO original and (2) CuO 60-min milled. c) TG curves for CeO_2 reduction under CO-TPR for (1) CeO_2 original and (2) CeO_2 60-min milled.

only one type of oxygen participates in the reduction process. The CO-TPR peak broadening depends on deviation in Ce-O and Cu-O bond strength due to structural defects introduced by mechanical stress.

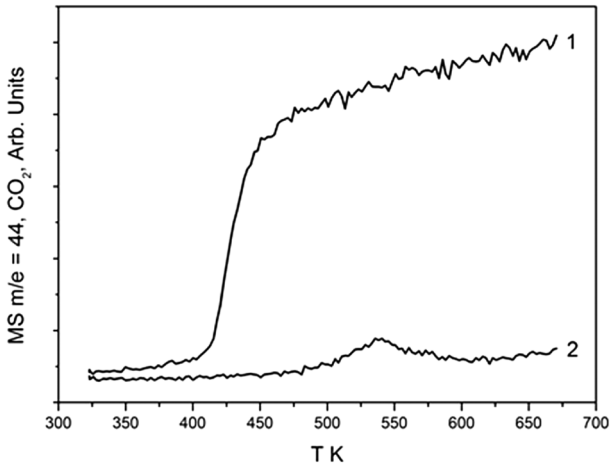

FIG. 4. CO-TPR. MS profile (m/e = 44, CO_2) for (1) CuO and (2) CeO_2 original powders.

B. Effect of milling conditions on structure, morphology, microstructure, and reducibility of the CuO-CeO_2 mixture

Figure 5 shows SEM micrographs of 10 wt.% Cu-CeO2 powders mixed in an agate mortar (original mixture) and milled for 60, 90 and 120 min. The powder morphology corresponds to changes in morphology of the major component, ceria. Small CeO_2 particles agglomerate together into large compact nanocomposites. In response, the powder specific surface area reduces progressively with increasing milling time. Remarkable compacting has taken place between 90 and 120 min of milling. The effect of milling conditions on structural parameters of 10 wt.% CuO-CeO_2 is shown in Table I.

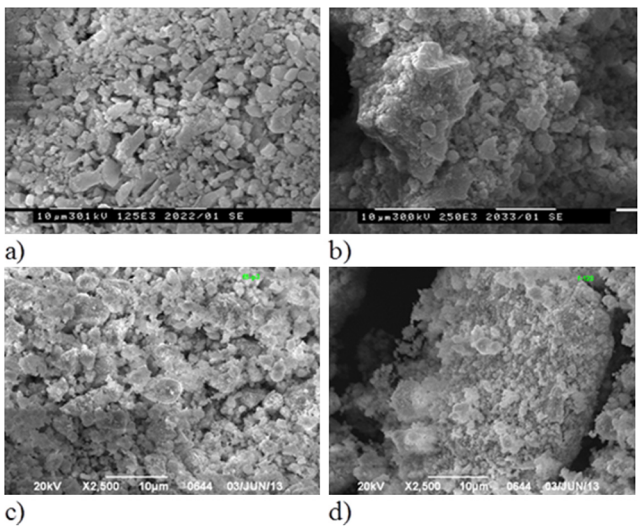

FIG. 5. SEM images of a) 10 wt.% CuO-CeO_2 powder mixed in agate mortar and milled for b) 60 min, c) 90 min, and d) 120 min.

Figure 6 shows XRD patterns of unmilled CuO-CeO_2 powders and powders milled for 30, 60, 90 and 120 min (samples 1, 2, 3 and 4, respectively). The fcc fluorite type CeO_2 and the monoclinic CuO are the only phases detected in the original and in as-milled powders (30, 60 and 90 min).

The CeO_2 peak shapes and positions are virtually independent of milling time. In spite of the powder particles becoming more compact, the CeO_2 crystallite size is in the range of 10 – 14 nm.

A broadening and a remarkable decrease in intensity of the CuO XRD peaks are observed with increasing milling time. After 120 min of milling, only CeO_2 peaks are present in the XRD pattern. According to the Scherrer equation, the CuO crystallite size reduces from 30 to 7 – 10 nm after 90 min of milling. Although no CuO phase is detected after 120 min of milling, AAS analysis shows that the Cu content is virtually constant.

The temperature programmed reduction technique (TPR) allows examining the oxygen state in oxide phases of different structure and morphology. In this study, H_2 and CO are used as probe molecules for oxygen state diagnostics in CuO-CeO_2 nanocomposites. The nanocomposite reducibility in H_2 and CO are described in terms of H_2O and CO_2 yield: the total H_2O or CO_2 amount formed during TPD runs are normalized to the powder mass or specific surface area. This parameter also characterizes direct participation of lattice oxygen in CO/H_2 oxidation.

Figure 7 shows H_2-TPR profiles for CuO and CuO-CeO_2 powders mixed in an agate mortar and milled for 30, 60, 90 and 120 min in terms of H_2O formation: i.e. changes in MS peak intensity recorded during H_2-TPR.

Figure 7a) shows MS (m/e = 18, H_2O) profiles for pure milled CuO and CuO mixed with CeO_2 without milling. The peak intensity is normalized to the CuO content. As mentioned above, no reduction of pure CeO_2 during H_2-TPR is observed. Thus, it is possible to compare reduction features for CuO powders with and without ceria. The total transformation CuO + H_2 → Cu + H_2O is achieved in both cases. The process goes as a single-step reduction (Rodriguez et al., 2003; Kim et al., 2003). Reduction of milled CuO starts approximately 50 K lower than that of CuO mixed with ceria, but proceeds much slower. Contrary to a broad TPR profile for milled pure CuO, a rather sharp and narrow TPR profile for the mixed CuO-CeO_2 powder is observed. The peak broadening depends both on powder size distribution and deviation in Cu-O bond strength due to structural defects introduced by mechanical stress, the concentration of which seems to be significantly higher in the case of pure CuO as compared to the CuO-CeO_2 mixture. Figure 7b) shows H_2-TPR MS profiles for CuO-CeO_2 powders milled for 30 – 120 min. The H_2-TPR curves are shifted to lower temperatures, as compared to pure CuO. Two-peak profiles with rather good MS peak division, see Figure 7b), are the special feature of these TPR spectra.

This means that at least two different independent processes are carried out during H_2-TPR in case of the milled CuO-CeO_2 samples, i.e. two different reactive oxygen loci are created under milling conditions. The low-temperature H_2-TPR peak percentage progressively increases from 16% to 30, 43 and 47% as milling time increases from 30 to 120 min. Heat release is also estimated for this peak on base of DSC and MS data (m/e = 18, H_2O). In contrast to the virtually unchanged heat release of about –70 kJ mol^{-1} H_2O found for the high-temperature process, it falls down from –321 to –176, –165 and –148 kJ mol^{-1} H_2O, while the milling time changes as

TABLE I. Effect of milling conditions on structural parameters of 10 mass% CuO-CeO_2.

Sample	Milling time [min]	CeO_2 Lattice const. [pm]	CeO_2 Crystallite size[a] [nm]	CuO Crystallite size[b] [nm]	CuO content[c] [wt.%]	Specific surface area [m^2/g]
CeO_2 original		541.1	~10			90
CeO_2 milled	60		~10			46.5
CuO-CeO_2 original		541.2	~16	~30	10	82
Sample 1	30	541.2	~10	~14	9.4	46
Sample 2	60	541.2	~12	~12	8	44
Sample 3	90	541.6	~11	~7	8	40.6
Sample 4	120	541.2	~13		0	20

[a]Calculated on base of Shelekhov and Sviridova (2000).
[b]Calculated by the Scherrer equation from the line broadening of CuO {111} peaks.
[c]Calculated from XRD spectra quantitative analysis (Yang et al., 2009).

30, 60, 90 and 120 min, respectively. H_2-TPR parameters are listed in Table II.

CO-TPR is an especially sensitive probe to discriminate and quantify various oxygen species in different CuO-CeO_2 structural composites such as surface or subsurface solid solutions (Liu and Flytzani-Stephanopoulos, 1995; Sedmak et al., 2003; and Galvita et al., 2014), CuO-CeO_2 dimeric structures (Kydd et al., 2009), monocrystals (Galvita et al., 2014), and/or CuO nanofragments distributed in CeO_2 matrix (Liu and Flytzani-Stephanopoulos, 1995; Wang et al., 2004; Luo et al., 2007; Wang et al., 2015; and Shang et al., 2017). Moreover, it gives direct information about a key step of CO-PROX reaction.

Figure 8 shows DSC, DTG and MS CO-TPR profiles for CuO-CeO_2 powders milled for 30, 60, 90 and 120 min. DSC and DTG profiles for CeO_2 milled without CuO for 60 min are also shown for comparison. MS data in Fig. 8c) are normalized to the sample weight. Peak positions were obtained by Gaussian fitting. As mentioned above, see Figure 4, CO-TPR profiles for CuO and CeO_2 both show single peak profiles. As can be seen in Fig. 8, three-to-four-peak profiles are observed for CuO-CeO_2 powders milled for 60 and 90 min. The TPR profile of the 120-min milled powder shows a different appearance: the low-temperature peak has the same

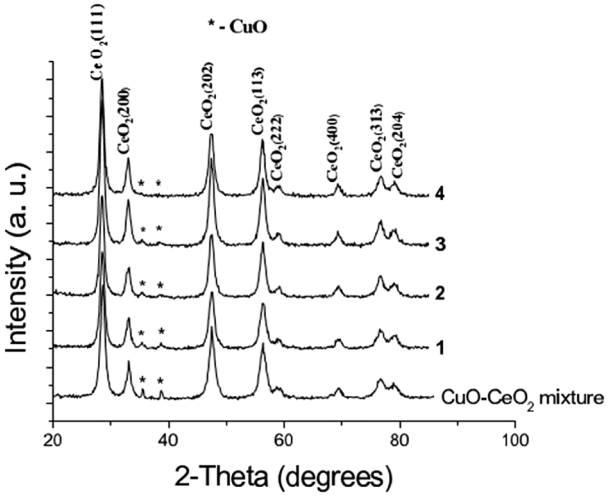

FIG. 6. XRD patterns of 10 wt.% CuO-CeO_2 powders milled for (1) 30 min (sample 1), (2) 60 min (sample 2), (3) 90 min (sample 3) and (4) 120 min (sample 4). For comparison, XRD pattern of original 10 wt.% CuO-CeO_2 mixture is added.

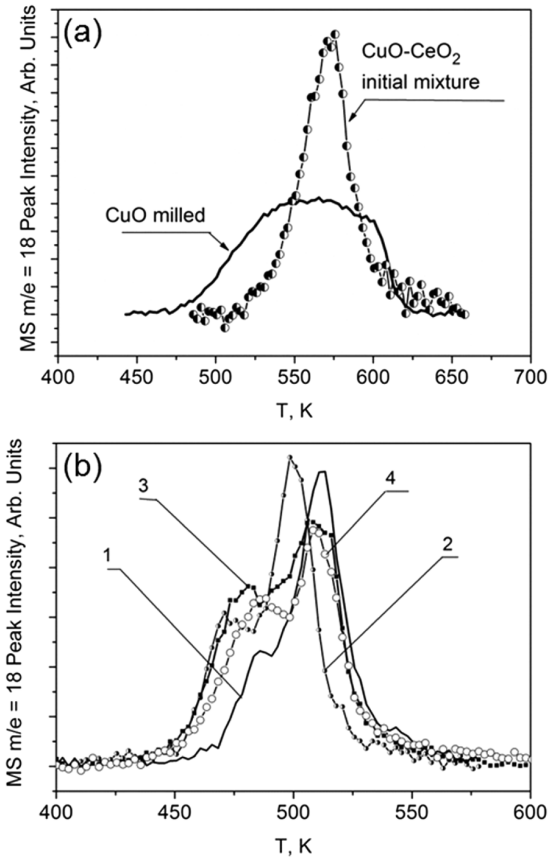

FIG. 7. H_2-TPR. MS profile (m/e = 18, H_2O) for (a) CuO as-milled and CuO–CeO_2 as-mixed and (b) CuO-CeO_2 powders milled for (1) 30 min, (2) 60 min, (3) 90 min and (4) 120 min.

TABLE II. H_2-TPR parameters. Experimental error of estimations is 10 – 15% due to MS calibration and DSC peak separation.

Sample/milling time	$CuO-CeO_2$ surface composition[a] [wt.%]	Low T T_{max} [K]	Low T MS peak fraction[b] [%]	Low T Q[c] [kJ/mol H_2O]	High T T_{max} [K]	High T MS peak fraction[b] [%]	High T Q[c] [kJ/mol H_2O]
CuO 60 min	100% CuO				566	100	−80
CuO/CeO_2 30 min	X% $CuO-CeO_2$	485.4	16.2	−321	513.4	83.8	−69
CuO/CeO_2 60 min	0.12% $CuO-CeO_2$	472.2	29.5	−176	498.5	70.5	−69
CuO/CeO_2 90 min	4.5% $CuO-CeO_2$	479.6	43.5	−165	508.4	56.5	−68
CuO/CeO_2 120 min	3.4% $CuO-CeO_2$	486.4	47.1	−148	508.4	52.9	−65

[a]Estimated on base of DSC-DTG-MS data in suggestion that the high-temperature peak belongs to reduction of Cu oxides.
[b]Calculated on base of Gaussian fitting of MS (m/e = 18, H_2O) curves.
[c]Calculated on base of Gaussian fitting of DSC and MS (m/e = 18, H_2O) curves.

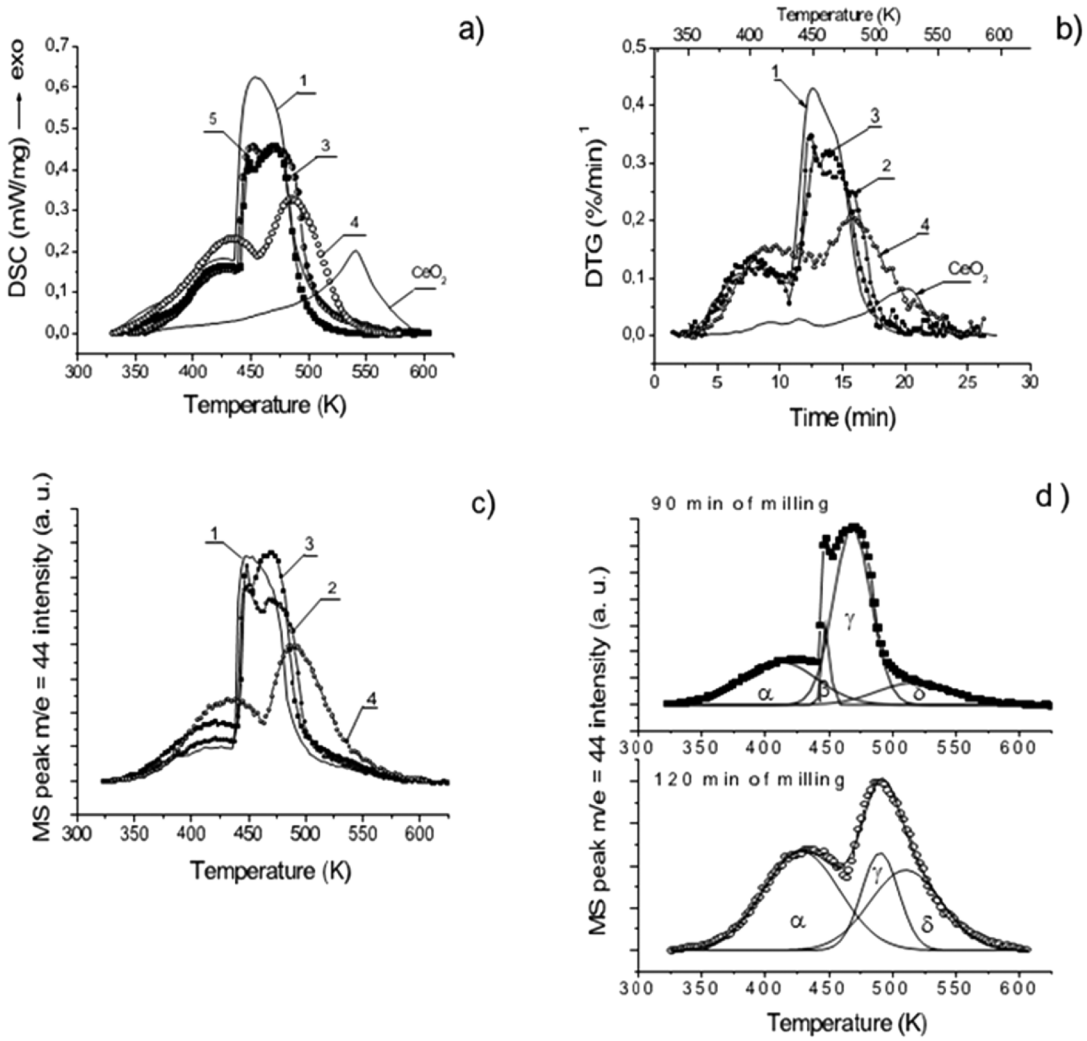

FIG. 8. CO-TPR profiles a) DSC, b) DTG and c) MS (m/e = 44, CO_2) for $CuO-CeO_2$ powders milled (1) 30 min. (2) 60 min, (3) 90 min and (4) 120 min in comparison with DSC and DTG curves for CeO_2 milled for 60 min. d) Gaussian fitting of MS profiles for 90- and 120-min milled $CuO-CeO_2$ powders. MS data are normalized to the sample weight.

TABLE III. CO-TPR parameters. Experimental error of estimations is 10 – 15% due to MS calibration and DSC peak separation.

Sample/milling time	α T_{max} [K]	α MS peak fraction[a] [%]	α Q[b] [kJ/mol H_2O]	β T_{max} [K]	β MS peak fraction[a] [%]	γ T_{max} [K]	γ MS peak fraction[a] [%]	δ T_{max} [K]	δ MS peak fraction[a] [%]
CuO 60 min								~691	100
CuO/CeO_2 30 min	~420	16.1	–182	~446	13.5	~464	70.4		
CuO/CeO_2 60 min	~421	19.6	–183	~449	12.3	~474	62. 0	~532	6.1
CuO/CeO_2 90 min	~426	26.4	–182	~448	5.5	~468	55.1	~516	13.0
CuO/CeO_2 120 min	~433	44.8	–195			~490	25	~513	30.2

[a]Calculated on base of Gaussian fitting of MS (m/e = 44, CO_2) curves.
[b]Calculated on base of Gaussian fitting of DSC and MS (m/e = 44, CO_2) curves.

position as that of the powders milled for 30 – 90 min (T_{max} = 420 – 430 K), but the high-temperature peaks are shifted to higher temperatures and merged into one. This hints on the fact that prolonged milling leads to dramatic changes in the CuO-CeO_2 nanocomposite microstructure. Unfortunately, XRD measurements give no information because no observable CuO peaks are detected in the corresponding pattern, see Figure 6. The low-temperature peak fraction progressively increases to about 16, 20, 26 and 45% while milling time increases from 30 to 120 min; a similar trend was found for the low-temperature H_2-TPR peak. However, contrary to H_2- TPR,

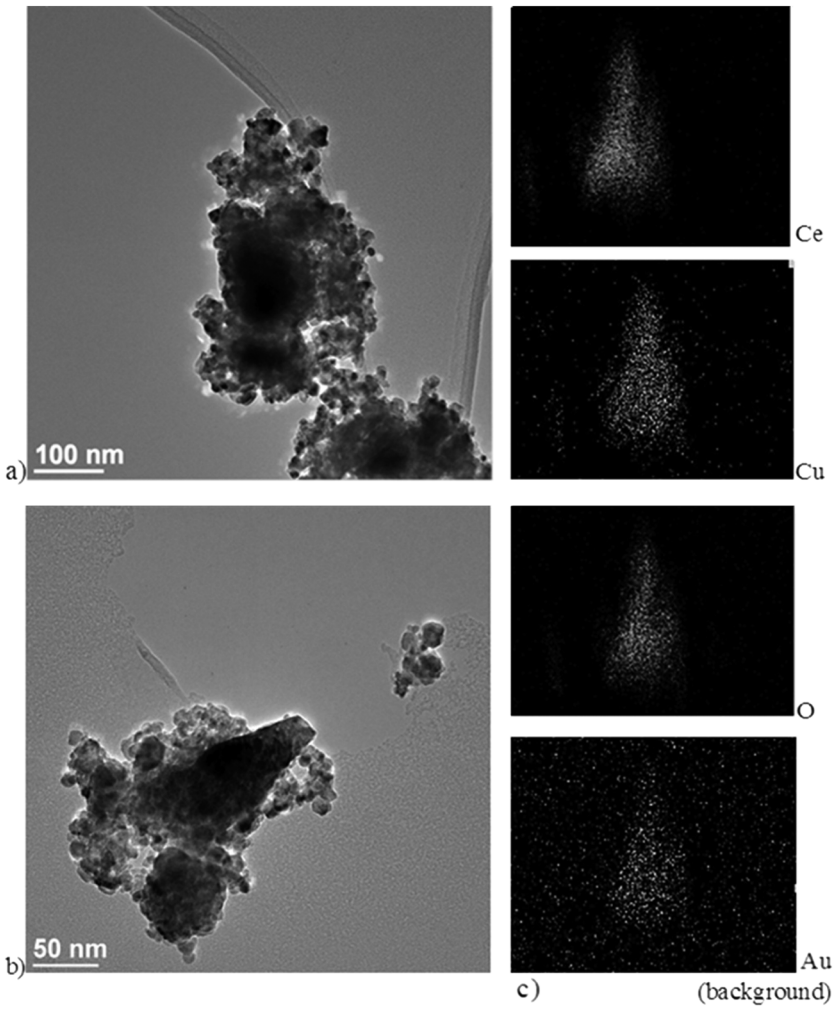

FIG. 9. TEM images of the CuO-CeO_2 mixture milled for a) 90 min, b) 120 min and c) elemental mapping of the particle depicted in Fig. 9b) obtained by EDS. Overview of the CuO-CeO_2 nanocomposite powder shows small crystallites sized about 10 nm gather in agglomerations of varying sizes. The individual crystallites seem to consist of CeO_2.

ΔH roughly estimated for the low-temperature oxygen extraction is virtually constant (ΔH = –182 kJ mol^{-1} CO_2). This value changes insignificantly in case of the 120-min milled powder (ΔH = –195 kJ mol^{-1} CO_2). It can be stated however that just like in the case of H_2-TPR, two to four different independent processes are carried out during CO-TPR in case of the milled CuO-CeO_2 samples; i.e. two to four different types of reactive oxygen loci are created under the milling. CO-TPR parameters are listed in Table III.

C. Effect of milling conditions on surface microstructure and oxidation states of surface elements

Fig. 9 shows TEM images of the CuO-CeO_2 mixture milled for a) 90 min, and b) 120 min, giving an overview of the CuO-CeO_2 nanocomposite powder: small crystallites sized about 10 nm gather in agglomerations of varying sizes. The individual crystallites seem to consist of CeO_2. Fig. 9c) shows elemental mapping of the particle depicted in Fig. 9b) obtained by EDS exhibiting a rather homogeneous distribution of highly dispersed Cu in the CeO_2 matrix; from EDS, it cannot be determined whether Cu is present in elemental form or as oxide. Figure 10 shows a HRTEM close-up of the CuO-CeO_2 mixture milled for 120 min. The particle surface seems to consist of randomly oriented and tightly interfaced CeO_2 crystallites. The most frequently observed crystal lattice spacings are labeled in Fig. 10 as spacing of CeO_2 (d_{111} = 0.311 – 0.316 nm, d_{200} = 0.268 nm, d_{110} = 0.300 nm). Direct measurements of lattice spacing in a Cu-rich region gives d = 0.304 nm corresponding to Cu_2O {110} planes. Neither lattice fringes corresponding to pure CuO, nor those of pure Cu could be detected. It should be noted that HRTEM images of the samples milled for shorter times look quite similar, and here too, only Cu_2O lattice fringes could be detected.

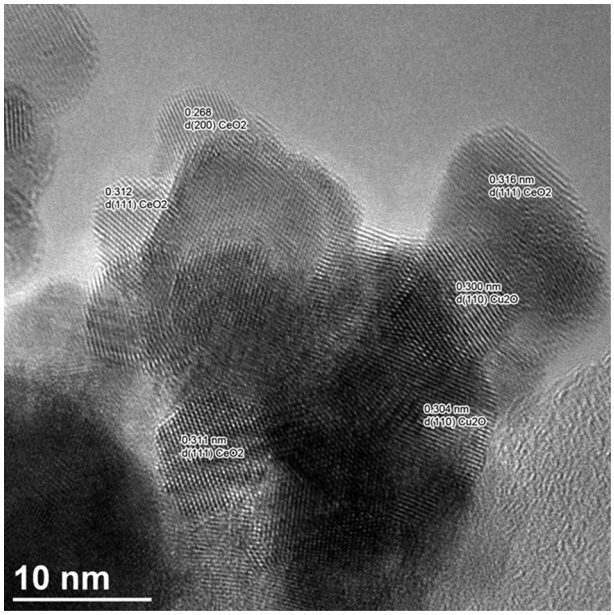

FIG. 10. HRTEM micrograph of 10 wt.% CuO-CeO_2 powder milled for 120 min with analysis of lattice spacing attributed to CeO_2 plane spacing and to d{110} Cu_2O.

In order to investigate the changes in the CuO-CeO_2 surface chemistry, XPS measurements were carried out, and are displayed in Fig. 11. XPS peaks corresponding to Cu *2p*, Ce *3d*, Ce *MNN*, O *1s*, Ce *4d* are present in a survey XPS spectrum of CuO-CeO_2

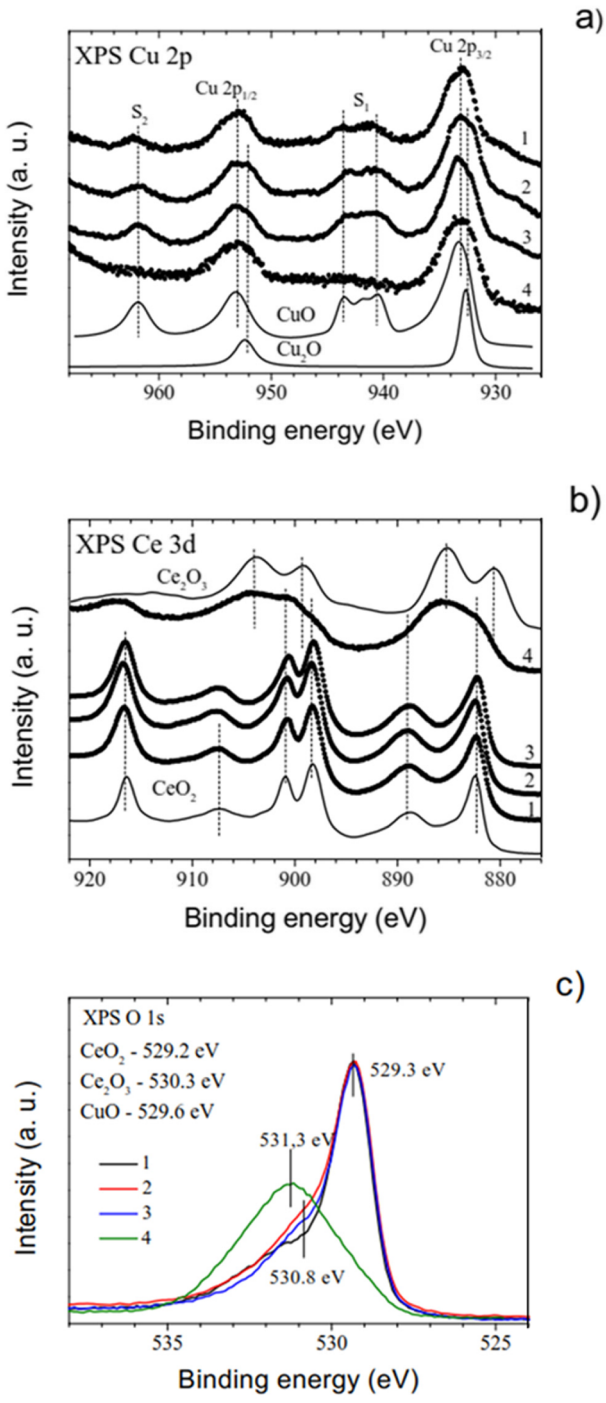

FIG. 11. XPS spectra a) Cu *2p* region, b) Ce *3d* region and c) O 1s region of CuO-CeO_2 powders milled for (1) 30 min, (2) 60 min, (3) 90 min and (4) 120 min.

powders milled for 30, 60, 90 and 120 min, respectively (not shown). No peaks corresponding to stainless steel from the ball-milling material were detected. Figure 11a) shows Cu *2p* spectra obtained from samples milled for 30 – 120 minutes in comparison with spectra of pure CuO and pure Cu_2O. The satellite structures S_1 and S_2 at binding energies of 962 and 941 – 944 eV confirm the presence of CuO in powders milled for 30 – 90 min. Concurrently, Cu_2O traces, the portion of which increases with milling time, are also present. The Cu $2p_{3/2}$ peak, exhibiting a slight shift of 1 eV when moving from Cu^{1+} (Cu_2O) to Cu^{2+} (CuO), is shifted by about another 1 – 2 eV in case of the sample milled for 90 min. A Cu_2O-like state with a complete loss of the satellites becomes dominant in the sample milled for 120 min. XPS data correlate with HRTEM results, see Fig. 10, where a lattice spacing of d = 0.304 nm, corresponding to Cu_2O {110} was found. Figure 11b) shows Ce *3d* spectra compared to those of pure CeO_2 and Ce_2O_3. As follows from comparison of Ce *3d* spectra of as-milled powders with spectra of CeO_2 and Ce_2O_3, only Ce^{4+} corresponding to CeO_2 is present on the surface of powders milled for 30 – 90 min. In contrast, dominantly Ce^{3+}, corresponding to Ce_2O_3, is detected on the surface of the powder milled for 120 min.

The O *1s* spectra of CuO-CeO_2 nanocomposites milled for different times are shown in Fig. 11c). The spectra are broad and consist of two overlapping peaks due to the presence of two chemical states of oxygen (Guzman et al., 2005; Xu et al., 2010). In addition to the main peak at 529.3 eV corresponding to lattice oxygen in Cu- and Ce-oxides, a shoulder at ~530.8 eV is present in spectra of powders milled for 30 – 90 min. The latter is usually attributed to highly polarized or weakly charged oxide ions at the surface and interface of nanocrystallites with unusually low coordination (Kullgren, 2012) or a mixture of hydroxyl groups on the surface of the catalysts (Song et al., 2016; Ren et al., 2017). This oxygen state is common for CuO-CeO_2 catalysts prepared by different methods (Xu et al., 2010; Kullgren, 2012; and Ren et al., 2017). The powder milled for 120 min dominantly contains surface oxygen, see Figure 11c), curve 4 (the curve with the peak situated to the left of the other three); the main peak position at 531.2 eV is in perfect agreement with 531.3 – 531. 5 eV attributed to oxygen on the surface of Cu-oxides and Cu-O films containing Cu^0 and Cu^{1+} (Park et al., 2011; Svintsitskiy et al., 2011).

D. Effect of milling conditions on nanocomposite catalytic properties

The catalytic activities for CO-PROX reaction of CeO_2 and series CuO-CeO_2 composites prepared by mechanochemical synthesis are shown in Fig. 12. The activity of pure CeO_2 is rather low: a CO conversion of only 30% at 623 K is observed. With the addition of 10 wt.% CuO and mixing in an agate mortar, the activity is slightly improved to a CO conversion of about 45% at 533 K. The catalytic activity increases progressively after milling the 10 wt.% CuO-CeO_2 mixtures for 30, 60 and 90 min, respectively. However, the composite milled for 120 min again shows less activity, comparable with that of 30-min milled powder. The CuO-CeO_2 composite milled for 90 min has the best catalytic properties: CO conversion of 97% at 423 K, which is in good agreement with properties of CuO-CeO_2 catalysts prepared by different methods. The catalyst phase composition was examined by XRD at maximal CO conversion (423 K) and at zero CO conversion (503 K). At maximal activity, the

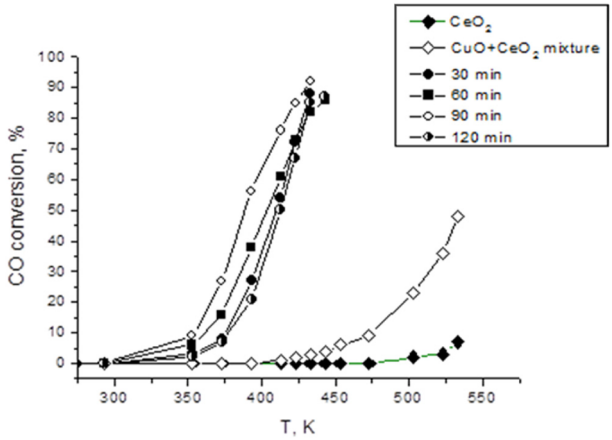

FIG. 12. CO conversion in CO_2 as a function of reaction temperature for CeO_2 milled for 60 min and CuO-CeO_2 powders mixed in agate mortar and milled for 30 – 120 min. Reaction conditions: 98 vol.% H_2, 1 vol.% CO and 1 vol.% O_2, a flow rate of 40 ml/min, 20 mg of the catalyst.

catalyst consists of 93 wt.% CeO_2, 4 wt.% CuO and 3 wt.% Cu. After the reaction, at 503 K, CuO was completely reduced: 92 wt.% CeO_2 and 8 wt.% Cu were detected. Redox cycles and catalytic activity cycles are reversible: the same CO conversion is reached after heating and cooling the samples subsequently several times.

IV. DISCUSSION

In a previous work, we studied the catalytic behavior of a Cu-CeO_2 nanocomposite produced by mechanochemical synthesis (Borchers et al., 2016). Similarities and differences between CuO-CeO_2 and Cu-CeO_2 nanocomposites will be discussed in the following.

Just as in case of the Cu-CeO_2 nanocomposite, ball milling is an effective and cheap method to produce CuO-CeO_2 nanocomposites suitable for preferential oxidation of CO in the presence of H_2; nanocomposites prepared by this simple technique are comparable in catalytic properties with catalysts synthesized by different traditional preparation methods such as wet impregnation, co-precipitation, sol-gel method, urea-nitrate combustion and hydrothermal methods (Yang et al., 2009; Prasad and Rattan, 2010; Maciel et al., 2012; and Cecilia et al., 2017). The CO conversion is as high as 97% at 423 K after milling for 90 min in case of CuO-CeO_2 nanocomposites, and 96% at 438 K after 60 min of milling in case of Cu-CeO_2 nanocomposites; the conversion is more or less the same, whereas the milling time to reach the highest conversion is longer for the CuO-CeO_2 nanocomposites; this will be discussed in detail further on.

The CuO-CeO_2 (or Cu-CeO_2) interaction is a necessary stage of the active CO-PROX catalyst formation; redox properties of CeO_2 modified by Cu ions are significantly different from those of CeO_2 alone, see Fig. 8a). First, pure CeO_2 exhibits a single-peak profile whereas the milled mixtures exhibit two to three peaks in both cases, and second, the peak temperature of about 570 K is more than 100 K higher than the high-T-peak of the mixtures. The CO-PROX reaction is obviously a strong evidence for the presence of an active

Cu-modified surface formed by close contact between the oxides. As can be seen in Figure 12, the intermixing of the original oxides in an agate mortar is already enough to create new active surface sites and increases the amount of CO conversion. The ball-milling treatment stimulates CuO-CeO_2 interaction: the catalytic activity in terms of CO conversion goes up, as the milling time changes from 30 to 90 min, corresponding to energy doses of 124 – 372 kJ mol^{-1}. After 120 min of milling, corresponding to an energy input of 496 kJ mol^{-1}, the activity reduces again and becomes comparable to the activity of the 30-min milled powder. The change in catalytic activity is accompanied by a drastic change in bulk and surface composition.

As shown in Fig. 6, no other phases except of the monoclinic phase CuO and the cubic phase CeO_2 are detected in XRD spectra of CuO-CeO_2 powders milled for 30 – 90 min. After 120 min of milling, only CeO_2 is observed in XRD. It seems that during mechanical treatment, only CuO is pulverized. While according to XRD results the CeO_2 crystallite size remains virtually unchanged, the CuO crystallite size changes from 30 to less than 7 nm after 90 min of milling. The disappearance of CuO XRD peaks after 120 min of milling is correlated with this trend. Thus, the high-energy ball milling results in CuO particle size reduction and in chemical reduction of CuO to Cu_2O, as well as in intermixing with CeO_2 powder, which in turn is rather stable in morphology.

The XPS and HRTEM results both give information about the subsurface and surface modification process. As shown by XPS, CuO and CeO_2 are predominantly present on the surfaces of samples milled for 30 – 60 min. Concurrently, Cu_2O traces, the portion of which increases with milling time, are also present. It is, as stated above, conspicuous that the Cu $2p_{3/2}$ peak, exhibiting a slight shift of 1 eV when moving from Cu^{1+} (Cu_2O) to Cu^{2+} (CuO), is shifted by about another 1 – 2 eV in case of the sample milled for 90 min. XPS studies of Cu^{3+} ions were performed by Healy et al. (1987), Teterin et al. (1991), and Kataoka et al. (2011). They report Cu $2p_{3/2}$ peak positions at 932.7 eV (Healy et al., 1987), 935.0 eV (Teterin et al., 1991), and 932.5 eV (Kataoka et al., 2011). However, Healy et al. (1987) state that "great care must be exercised when interpreting XPS studies of copper compounds in formal +2 or +3 oxidation states . . .surface specific effects were significant and this may be a general characteristic of Cu(III) compounds". Recently, Elias et al. (2014; 2016; and 2017), after close examination of $Cu_yCe_{1-y}O_2$ and CuO + $Cu_yCe_{1-y}O_2$, came to the conclusion that the most active species in catalysis are Cu^{3+} situated near the CeO_2 surface. In view of the observed Cu $2p_{3/2}$ peak shift observed in case of the sample milled for 90 min, it cannot be excluded that this peak shift is due to the presence of Cu^{3+} on the surface of this sample, or nearby. On the other hand, Harrison et al. (2000) found that promotion of ceria with Cu^{2+} enhances the activity toward oxidation of CO, while Martínez-Arias et al. (2013) as well as Ding et al. (2018) state that the most active sites for CO oxidation reaction are Cu^{1+} species originating from partially reduced CuO. In the context of this work, it cannot be decided conclusively whether Cu^{1+}, Cu^{2+}, or Cu^{3+} are the active species; it can however be stated that most probably not the oxide CuO but Cu ions are causal for CO-PROX, both in case of the CuO-CeO_2 and the Cu-CeO_2 nanocomposites; this is a significant similarity between both.

Another observation, which is in agreement with H_2- and CO-TPR data, is the appearance of a new oxygen state detected as a shoulder of the main peak at 530.8 eV, see Fig. 11. As stated by Kataoka et al. (2011), the maximum depth of XPS analysis is about 10 nm. For the CeO_2 lattice, such a surface/subsurface layer is 17 – 18 unit cells thick. The concentration of Cu ions distributed in a subsurface CeO_2 layer was roughly calculated on base of CO-TPR data assuming that the distribution is uniform. For the 90 min milled powder with the best catalytic properties it gives 1 Cu ion per 7 unit cells. It can however be assumed that the Cu dopant concentration follows a gradient, steep near the surface, and increasingly flat with increasing distance from the surface; this is corroborated by Gamarra et al. (2007). In the sample milled for 120 min, surface oxygen as well as Cu^{1+} and Ce^{3+} become dominant. The presence of Cu_2O supports the conclusion of Palkar et al. (1996) about the preferential stability of small Cu_2O crystals as compared to CuO. The appearance of Ce^{3+} can be explained by a significant reconstruction of the most stable {111} surface of CeO_2 in the presence of subsurface oxygen vacancies: the upper layers resemble the Ce_2O_3 (0001) surface and "the structure could represent a precursor to the phase transition of CeO_2 to Ce_2O_3" (Fronzi et al., 2009). The surface microstructure of 90- and 120 min milled CuO-CeO_2 powders is shown in HRTEM images (Fig. 10). It is important to note that no individual CuO nanofragments are detected. Direct measurements of lattice spacings in a Cu-rich region gives d = 300 – 304 pm corresponding to Cu_2O {110} planes. The Cu_2O nanofragments sized about 5 nm detected on the surface are in good agreement with the XPS results. HRTEM-based calculations also clarify the local structure of CeO_2 doped with CuO, which is different from the bulk CeO_2. In line with numerous publications, where variations in CeO_2 cell dimension are discussed (Wang et al., 2005; Luo et al., 2007; Kehoe et al., 2011; Lu et al., 2011; Vanpoucke et al., 2014; and Wu et al., 2015), both cell expansion and cell contraction could be observed. On the one hand, a replacement of Ce^{4+} (92 pm) ions by smaller Cu ions (74 pm for Cu^{2+}) could be responsible for the lattice contraction; on the other hand, Cu ion incorporation is accompanied by a reorganization of the ceria lattice and the formation of charge compensating oxygen vacancies, leading to larger Ce^{3+} ions (115 pm), resulting in a lattice expansion. Additionally, {111}-terminated ceria nanocrystals exhibit a lattice expansion because they are always cerium rich and concurrently reduced (Kullgren, 2012). The high local surface pressure caused by ball collisions might be another reason for the CeO_2 lattice contraction (Streletskii, 1991; Wang et al., 2014). The only observed difference is between the surface morphologies of the 90- and 120-min milled powders. In case of the latter, CeO_2 {200} planes with d_{200} = 266 – 272 pm are detected in addition to the dominant CeO_2 {111} planes with d_{111} = 311 – 316 pm. This hints on a further degradation of CeO_2 crystallites under prolonged ball-milling. Thus, HRTEM images directly demonstrate that both nanocomposite surfaces consist of CeO_2 nanocrystallites doped with Cu ions, corroborating the results discussed above concerning the active species in CO-PROX. Just as in case of the Cu-CeO_2 nanocomposite, one can assume that the excellent catalytic properties of the CuO-Ce_2O catalysts are due to the fact that the formation energy of oxygen vacancies in CeO_2, E_{vac}, is considerably reduced in the presence of Cu (Lu et al., 2011). Additionally, Martínez-Arias et al. (2013), Monte et al. (2014) as well as Yang et al. (2010) found interfacial Cu-carbonyls as active sites, and Kydd et al. (2009) found that adsorbate molecules of CO possess orbitals that interact with Cu

3d orbitals, whereas the contracted nature of Ce *4f* orbital creates poor orbital overlaps. They also state that CO oxidation occurs via the Mars-van Krevelen mechanism, where CO is adsorbed onto Cu cations, and surface oxygen is abstracted to yield CO_2, and similar for H_2 oxidation. The main difference is "as H_2 is nonpolar, it must undergo dissociation prior to reaction. Conversely, the nucleophilic nature of CO means it will readily adsorb onto cationic Cu sites at the catalyst surface. As a result, catalysts containing ionic Cu-oxygen bonds at the surface display high levels of activity and selectivity to CO oxidation at low reaction temperatures" (Kydd et al., 2009).

There are three main differences between the CuO-CeO_2 and the Cu-CeO_2 nanocomposites: the milling time to attain the highest catalytic activity is longer in case of CuO-CeO_2 than in case of Cu-CeO_2, the peak temperatures are somewhat higher: T_{max} = 426 K (CuO-CeO_2) vs. T_{max} = 395 K (Cu-CeO_2), both are the low-*T*-peaks, and last, but not least, TPR of CuO-CeO_2 exhibits four peaks after 90 min of milling, see Fig. 8d), while Cu-CeO_2 only has two (Borchers et al., 2016). The reason for the longer milling time of the CuO-CeO_2 nanocomposite is most probably the necessity for the CuO to decompose: 156 kJ mol^{-1} have to be made available (Knacke et al., 1991), which is not a problem with energy doses of 248, 372 and 496 kJ mol^{-1} after 60, 90, and 120 min of milling; it might only take some extra milling time. The elevated temperature of the low-*T*-peak might be due to the fact that after 60 and 90 minutes of milling, there still is some CuO as can be seen in Fig. 6; assuming that some of this CuO has to be reduced before CO oxidation, the necessary energy input would explain the temperature rise as compared to Cu-CeO_2. The fact that there are four peaks during CO-TPR can easily be explained according to Lu et al. (2011): In a density functional theory (DFT) study they find four different oxygen vacancy formation energies E_{vac}, depending on whether the first O vacancy is in NN or NNN position of Cu, and whether the vacancy is directly on the surface or not; the values are 0.98 eV (NN pos., bulk), 0.67 eV (NN pos., surf.), 0.30 eV (NNN pos., bulk), and 0.04 eV (NNN pos., surf.). However, Paier et al. (2013) state that "for a vacancy in CeO_2 there are many different possibilities. . . even more possibilities exist when dopants are involved," doubting the reliability of DFT calculations in this system. Four reaction mechanisms seem plausible, however; in case of the Cu-CeO_2 catalysts it was perhaps not possible to distinguish four peaks because of overlap.

The last open question is: why is the performance of the sample milled for 90 minutes so much better than that of the one milled for 120 minutes? The first was found to be the best catalyst, the second lost activity in low-temperature CO oxidation. However, there is evidence that the nanocomposite milled for 120 min should in principle be the best catalyst: (i) the fraction of reactive oxygen participating in low-temperature CO oxidation is 46.8% instead of 26.4%, see Table III; (ii) the low-coordinated surface oxygen is the dominant oxygen state, see Fig. 11c). In both cases the nanocomposite surface microstructure is very similar. They consist of CeO_2 nanocrystals with dominant CeO_2{111} planes modified by Cu ions, see Fig. 10. Additionally, the powders contain Cu_2O, which is supposed to be the most important component of active CuO-CeO_2 catalysts. Nevertheless, the catalytic properties declined markedly, see Fig. 12. There is only one explanation for this phenomenon: the cuprous oxide fraction seems to grow substantially when milled for longer times than 90 min; Cu_2O blocks the CeO_2 surface, the area of which decreases. According to Svintsitskiy et al. (2013), the Cu_2O surface layer can be considered as a layer of approximately 9 nm thickness. In such a case, the surface works mainly as a Cu_2O surface, which is also suitable for CO oxidation, but not in the presence of H_2. It is well known that when Cu, Cu_2O, and CuO are compared without the addition of CeO_2, the activity of CO oxidation is highest for Cu_2O especially at lower temperatures like 413 K, where Cu and CuO show no activity at all (Huang and Tsai, 2003). Nanocrystalline Cu_2O can easily be reduced to Cu metal which significantly stimulates H_2 oxidation at lower temperatures. Additionally, the activity of pure copper oxide in terms of CO oxidation is lower, as compared to CuO-CeO_2 materials. Thus, the role of highly dispersed, partially reduced copper oxide in CO-PROX reaction is clearly shown. Cu^{1+}, Cu^{2+} and perhaps Cu^{3+} ions are very important for CO-PROX activity as dopants to the CeO_2 surface.

V. CONCLUSIONS

Nanocomposite CuO-CeO_2 catalyst for CO-PROX reaction was prepared by mechanochemical synthesis from individual oxides. The catalytic properties were controlled by mechanical energy transmitted to the nanocomposite depending on milling time. The catalyst surface consists of {111}-terminated CeO_2 nanofragments, which are doped by Cu^{1+}, Cu^{2+} and perhaps Cu^{3+} ions and/or affected by high local pressure due to ball collisions. Cu^{2+} and Ce^{4+} both are detected on the active catalyst surface. Final dispersion of CuO after 120 min of milling into the CeO_2 matrix results in a pronounced decline of catalytic activity due to blocking of the CeO_2 surface by Cu_2O.

To conclude, ball milling has proven to be a successful, simple, and low-cost method to synthesize CuO-CeO_2 catalysts for preferential oxidation of CO in the presence of H_2.

ACKNOWLEDGMENTS

This work was partially supported by Russian Foundation for Basic Research [Projects n.n. 16-03-00330a and 16-03-00178a] in theoretical studies and part of experimental research and by FASO [program no. AAAA-A18-118012390374-3]. XPS measurements were supported by FASO (Theme "Electron"). The Alexander von Humboldt foundation is gratefully acknowledged for funding. We also would like to thank N. Berezkina for SEM measurements. We acknowledge support by the Open Access Publication Funds of the Göttingen University.

Declarations of interest: none.

REFERENCES

Avgouropoulos, G., Ioannides, T., Papadopoulou, C., Batista, J., Hocevar, S., and Matralis, H. K., "A comparative study of Pt/γ-Al_2O_3, Au/α-Fe_2O_3 and CuO–CeO_2 catalysts for the selective oxidation of carbon monoxide in excess hydrogen," Catal. Today **75**, 157–167 (2002).

Borchers, C., Martin, M. L., Vorobjeva, G. A., Morozova, O. S., Firsova, A. A., Leonov, A. V., Kurmaev, E. Z., Kukharenko, A. I., Zhidkov, I. S., and Cholakh, S. O., "Cu-CeO_2 nanocomposites: Mechanochemical synthesis, physico-chemical properties, CO-PROX activity," J. Nanopart. Res. **18**, 344–359 (2016).

Cecilia, J. A., Arango-Díaz, A., Marrero-Jerez, J., Núñez, P., Moretti, E., Storaro, L., and Rodríguez-Castellón, E., "Catalytic behaviour of CuO-CeO_2 systems prepared by different synthetic methodologies in the CO-PROX reaction under CO_2-H_2O feed stream," Catalysts **7**, 160–180 (2017).

Ding, J., Li, L., Li, H., Chen, S., Fang, S., Feng, T., and Li, G., "Optimum preferential oxidation performance of CeO_2–CuO_x–RGO composites through interfacial regulation," ACS Appl. Mater. Interfaces **10**, 7935–7945 (2018).

Elias, J. S., Artrith, N., Bugnet, M., Giordano, L., Botton, G. A., Kolpak, A. M., and Shao-Horn, Y., "Elucidating the nature of the active phase in copper/ceria catalysts for CO oxidation," ACS Catal. **6**, 1675–1679 (2016).

Elias, J. S., Risch, M., Giordano, L., Mansour, A. N., and Shao-Horn, Y., "Structure, bonding, and catalytic activity of monodisperse, transition-metal-substituted CeO_2 nanoparticles," J. Am. Chem. Soc. **136**, 17193–17200 (2014).

Elias, J. S., Stoerzinger, K. A., Hong, W. T., Risch, M., Giordano, L., Mansour, A. N., and Shao-Horn, Y., "In situ spectroscopy and mechanistic insights into CO oxidation on transition-metal-substituted ceria nanoparticles," ACS Catal. **7**, 6843–6857 (2017).

Fronzi, M., Soon, A., Delley, B., Traversa, E., and Stampfl, C., "Stability and morphology of cerium oxide surfaces in an oxidizing environment: A first-principles investigation," J. Chem. Phys. **131**, 104701 (2009).

Galvita, V. V., Filez, M., Bliznuk, V., and Marin, G. B., "The role of different types of CuO in CuO–CeO_2/Al_2O_3 for total oxidation," Catal. Lett. **144**, 32–43 (2014).

Gamarra, D., Munuera, G., Hungria, A. B., Fernández-García, M., Conesa, J. C., Midgley, P. A., Wang, X. Q., Hanson, J. C., Rodriguez, J. A., and Martínez-Arias, A., "Structure-activity relationship in nanostructured copper-ceria-based preferential CO oxidation catalysts," J. Phys. Chem. C **111**, 11026–11038 (2007).

Guzman, J., Carrettin, S., Fierro-Gonzalez, J. C., Hao, Y., Gates, B. C., and Corma, A., "CO oxidation catalyzed by supported gold: Cooperation between gold and nanocrystalline rare-earth supports forms reactive surface superoxide and peroxide species," Angew. Chem. Int. Ed. **44**, 4778–4781 (2005).

Harrison, P. G., Ball, I. K., Azelee, W., Daniell, W., and Goldfarb, D., "Nature and surface redox properties of copper(II)-promoted cerium(IV) oxide CO-oxidation catalysts," Chem. Mater. **12**, 3715–3725 (2000).

Healy, P. C., Myhra, S., and Stewart, A. M., "XPS studies of planar four-coordinate copper (II) and copper(III) complexes," Jpn. J. Appl. Phys. **26**, L1884–L1887 (1987).

Hossain, S. T., Azeeva, E., Zhang, K., Zell, E. T., Bernard, D. T., Balaz, S., and Wang, R., "A comparative study of CO oxidation over Cu-O-Ce solid solutions and CuO/CeO_2 nanorods catalysts," Appl. Surf. Sci. **455**, 132–143 (2018).

Huang, T.-J. and Tsai, D.-H., "CO oxidation behavior of copper and copper oxides," Catal. Lett. **87**, 173–178 (2003).

Il'ichev, A. N., Firsova, A. A., and Korchak, V. N., "Mechanism of CO oxidation in excess H_2 over CuO/CeO_2 catalysts: ESR and TPD studies," Kinet. Catal. **47**, 585–592 (2006).

Jing, G., Zhang, L., Ma, Y., Wu, J., Wang, Q., Yan, L., and Zeng, S., "Comparison of Au–Ce and Au–Cu interaction over Au/CeO_2–CuO catalysts for preferential CO oxidation," ChrystEngComm **21**, 363–371 (2019).

Kataoka, T., Yamazaki, Y., Singh, V. R., Fujimori, A., Chang, F.-H., Lin, H.-J., Huang, D. J., Chen, C. T., Xing, G. Z., Seo, J. W., Panagopoulos, C., and Wu, T., "Ferromagnetic interaction between Cu ions in the bulk region of Cu-doped ZnO nanowires," Phys. Rev. B **84**, 153203 (2011).

Kehoe, A. B., Scanlon, D. O., and Watson, G. W., "Role of lattice distortions in the oxygen storage capacity of divalently doped CeO_2," Chem. Mater. **23**, 4464–4468 (2011).

Kim, J. Y., Rodriguez, J. A., Hanson, J. C., Frenkel, A. I., and Lee, P. L., "Reduction of CuO and Cu_2O with H_2: H embedding and kinetic effects in the formation of suboxides," J. Am. Chem. Soc. **125**, 10684–10692 (2003).

Kim, K.-Y., Han, J., Nam, S. W., Lim, T.-H., and Lee, H.-I., "Preferential oxidation of CO over CuO/CeO_2 and Pt-Co/Al_2O_3 catalysts in micro-channel reactors," Catal. Today **131**, 431–436 (2008).

Knacke, O., Kubaschewski, O., and Hesselmann, K., *Thermochemical Properties of Inorganic Substances* (Springer, Berlin, 1991).

Kullgren, J., "Oxygen vacancy chemistry in ceria, digital comprehensive summaries," Ph.D. Thesis, Uppsala Dissertations from the Faculty of Science and Technology 896, Acta Universitatis Upsaliensis, Uppsala (2012).

Kydd, R., Teoh, W. Y., Wong, K., Wang, Y., Scott, J., Zeng, Q.-H., Yu, A.-B., Zou, J., and Amal, R., "Flame-synthesized ceria-supported copper dimers for preferential oxidation of CO," Adv. Funct. Mater. **19**, 369–377 (2009).

Li, J., Zhu, P., Zuo, S., Huang, Q., and Zhou, R., "Influence of Mn doping on the performance of CuO-CeO_2 catalysts for selective oxidation of CO in hydrogen-rich streams," Appl. Catal. A **381**, 261–266 (2010).

Liu, L. and Corma, A., "Metal catalysts for heterogeneous catalysis: From single atoms to nanoclusters and nanoparticles," Chem. Rev. **118**, 4981–5079 (2018).

Liu, W. and Flytzani-Stephanopoulos, M., "Total oxidation of carbon monoxide and methane over transition metal fluorite oxide composite catalysts: I. Catalyst composition and activity," J. Catal. **153**, 304–316 (1995).

Liu, W. and Flytzani-Stephanopoulos, M., "Transition metal-promoted oxidation catalysis by fluorite oxides: A study of CO oxidation over Cu-CeO_2," Chem. Engr. **64**, 283–294 (1996).

Lu, Z., Yang, Z., He, B., Castleton, C., and Hermansson, K., "Cu-doped ceria: Oxygen vacancy formation made easy," Chem. Phys. Lett. **510**, 60–66 (2011).

Luo, M.-F., Song, Y.-P., Lu, J.-Q., Wang, X.-Y., and Pu, Z.-Y., "Identification of CuO Species in high surface area CuO–CeO_2 catalysts and their catalytic activities for CO oxidation," J. Phys. Chem. C **111**, 12686–12692 (2007).

Maciel, C. G., de Freitas Silva, T., Hirooka, M. I., Belgacem, M. N., and Assaf, J. M., "Effect of nature of ceria support in CuO/CeO_2 catalyst for PROX-CO reaction," Fuel **97**, 245–252 (2012).

Maciel, C. G., Profeti, L. P. R., Assaf, E. M., and Assaf, J. M., "Hydrogen purification for fuel cell using CuO/CeO_2–Al_2O_3 catalyst," J. Power Sources **196**, 747–753 (2011).

Martínez-Arias, A., Gamarra, D., Hungría, A. B., Fernández-García, M., Munuera, G., Hornés, A., Bera, P., Conesa, J. C., and Cámara, A. L., "Characterization of active sites/entities and redox/catalytic correlations in copper-ceria-based catalysts for preferential oxidation of CO in H_2-ich streams," Catalysts **3**, 378–400 (2013).

Monte, M., Gamarra, D., Cámara, A. L., Rasmussen, S. B., Gyorffy, N., Schay, Z., Martínez-Arias, A., and Cones, J. C., "Preferential oxidation of CO in excess H_2 over CuO/CeO_2 catalysts: Performance as a function of the copper coverage and exposed face present in the CeO_2 support," Catal. Today **229**, 104–113 (2014).

Paier, J., Penschke, C., and Sauer, J., "Oxygen defects and surface chemistry of ceria: Quantum chemical studies compared to experiment," Chem. Rev. **113**, 3949–3985 (2013).

Palkar, V. R., Ayyub, P., Chattopadhyay, S., and Multani, M., "Size-induced structural transitions in the Cu-O and Ce-O systems," Phys. Rev. B **53**, 2167–2171 (1996).

Park, J.-Y., Lim, K.-A., Ramsier, R. D., and Kang, Y.-C., "Spectroscopic and morphological investigation of copper oxide thin films prepared by magnetron sputtering at various oxygen ratios," Bull. Korean Chem. Soc. **32**, 3395–3399 (2011).

Polster, C. S., Nair, H., and Baertsch, C. D., "Study of active sites and mechanism responsible for highly selective CO oxidation in H_2 rich atmospheres on a mixed Cu and Ce oxide catalyst," J. Catal. **266**, 308–319 (2009).

Prasad, R. and Rattan, G., "Preparation methods and applications of CuO-CeO_2 catalysts: A short review," Chem. React. Engr. & Catal. **5**, 7–30 (2010).

Qi, X. and Flytzani-Stephanopoulos, M., "Activity and stability of Cu-CeO_2 catalysts in high-temperature water-gas shift for fuel-cell applications," Ind. Engr. Chem. Res. **43**, 3055–3306 (2004).

Ren, Z., Li, J., Peng, F., Liang, X., and Chen, B., "Morphology-dependent properties of Cu/CeO_2 catalysts for the water-gas shift reaction," Catalysts **7**, 48–60 (2017).

Rodriguez, J. A., Kim, J. Y., Hanson, J. C., Pérez, M., and Frenkel, A. I., "Reduction of CuO in H_2: *In situ* time-resolved XRD studies," Catal. Lett. **85**, 247–254 (2003).

Scherrer, P., "Bestimmung der Größe und der inneren Struktur von Kolloidteilchen mittels Röntgenstrahlen," Nachrichten von der Gesellschaft der Wissenschaften zu Göttingen, Mathematisch-Physikalische Klasse **2**, 98–100 (1918) (in German).

Sedmak, G., Hočevar, S., and Levec, J., "Kinetics of selective CO oxidation in excess of H_2 over the nanostructured $Cu_{0.1}Ce_{0.9}O_{2-y}$ catalyst," J. Catal. **213**, 135–150 (2003).

Senanayake, S. D., Stacchiola, D., and Rodriguez, J. A., "Unique properties of ceria nanoparticles supported on metals: Novel inverse ceria/copper catalysts for CO oxidation and the water-gas shift reaction," Acc. Chem. Res. **46**, 1702–1711 (2013).

Shang, H., Zhang, X., Xu, J., and Han, Y., "Effects of preparation methods on the activity of CuO_2 catalysts for CO oxidation," Front. Chem. Sci. Engr. **11**, 603–612 (2017).

Shapovalov, V. and Metiu, H., "Catalysis by doped oxides: CO oxidation by $Au_xCe_{1-x}O_2$," J. Catal. **245**, 205–214 (2007).

Shelekhov, E. V. and Sviridova, T. A., "Programs for x-ray analysis of polycrystals," Met. Sci. Heat Treat. **42**, 309–313 (2000).

Song, C., Li, H., Wang, D., and Yang, Y., "CeO_2 decorated CuO hierarchical composites as inverse catalyst for enhanced CO oxidation," RSC Adv. **6**, 102931 (2016).

Streletskii, A. N., "Elastic energy relaxation in mechanochemical processes," Dr. of Sci. Thesis, Semenov Institute of Chemical Physics RAS, Moscow (in Russian) (1991).

Svintsitskiy, D. A., Chupakhin, A. P., Slavinskaya, E. M., Stonkus, O. A., Stadnichenko, A. I., Koscheev, S. V., and Boronin, A. I., "Study of cupric oxide nanopowders as efficient catalysts for low-temperature CO oxidation," J. Mol. Catal. A **368-369**, 95–106 (2013).

Svintsitskiy, D. A., Stadnichenko, A. I., Demidov, D. V., Koscheev, S. V., and Boronin, A. I., "Investigation of oxygen states and reactivities on a nanostructured cupric oxide surface," Appl. Surf. Sci. **257**, 8542–8549 (2011).

Tang, X., Zhang, B., Li, Y., Xu, Y., Xin, Q., and Shen, W., "CuO/CeO_2 catalysts: Redox features and catalytic behaviors," Appl. Catal. A **288**, 116–125 (2005).

Teterin, Y. A., Sosulnikov, M. I., Ozhogin, V. I., Senschenkova, T. M., Tolmacheva, N. S., and Shustov, L. D., "XPS studies of Cu^{3+} ions in $Ba(CuO_2)_2nH_2O$," Physica C **185-189**, 837–838 (1991).

Vanpoucke, D. E. P., Bultinck, P., Cottenier, S., Van Speybroeck, V., and Van Driessche, I., "Aliovalent doping of CeO_2: DFT study of oxidation state and vacancy effects," J. Mater. Chem. A **2**, 13723–13737 (2014).

Wang, Q., He, D., Peng, F., Lei, L., Liu, P., Yin, S., Wang, P., Xu, C., and Liu, J., "Unusual compression behavior of nanocrystalline CeO_2," Sci. Rep. **4**, 4441 (2014).

Wang, W. W., Du, P. P., Zou, S. H., He, H. Y., Wang, R. X., Jin, Z., Shi, S., Huang, Y. Y., Si, R., Song, Q. S., Jia, C. J., and Yan, C. H., "Highly dispersed copper oxide clusters as active species in copper-ceria catalyst for preferential oxidation of carbon monoxide," ACS Catalysis **5**, 2088–2099 (2015).

Wang, X., Hanson, J. C., Frenkel, A. I., Kim, J.-Y., and Rodriguez, J. A., "Time-resolved studies for the mechanism of reduction of copper oxides with carbon monoxide: Complex behavior of lattice oxygen and the formation of suboxides," J. Phys. Chem. B **108**, 13667–13673 (2004).

Wang, X., Rodriguez, J. A., Hanson, J. C., Gamarra, D., Martínez-Arias, A., and Fernández-García, M., "Unusual physical and chemical properties of Cu in $Ce_{1-x}Cu_xO_2$ oxides," J. Phys. Chem. B **109**, 19595–19603 (2005).

Wongkaew, A., Kongsi, W., and Limsuwan, P., "Physical properties and selective CO oxidation of coprecipitated CuO/CeO_2 catalysts depending on the CuO in the samples," Adv. Mat. Sci. Engr. **2013**, 1.

Wu, T. S., Li, H. D., Chen, Y. W., Chen, S. F., Su, Y. S., Chu, C. H., Pao, C. W., Lee, J. F., Lai, C. H., Jeng, H. T., Chang, S. L., and Soo, Y. L., "Unconventional interplay between heterovalent dopant elements: Switch-and-modulator band-gap engineering in (Y, Co)-Codoped CeO_2 nanocrystals," Sci. Rep. **5**, 15415 (2015).

Xu, J., Harmer, J., Li, G., Chapman, T., Collier, P., Longworth, S., and Tsang, S. C., "Size dependent oxygen buffering capacity of ceria nanocrystals," Chem. Commun. **46**, 1887–1889 (2010).

Yang, W., Li, D., Xu, D., and Wang, X., "Effect of CeO_2 preparation method and Cu loading on CuO/CeO_2 catalysts for methane combustion," J. Energy Chem. **18**, 458–466 (2009).

Yang, Z., He, B., Lu, Z., and Hermansson, K., "Physisorbed, chemisorbed, and oxidized CO on highly active Cu-CeO_2 (111)," J. Phys. Chem. C **114**, 4486–4494 (2010).

Yao, S. Y., Xu, W. Q., Johnston-Peck, A. C., Zhao, F. Z., Liu, Z. Y., Luo, S., Senanayake, S. D., Martínez-Arias, A., Liu, W. J., and Rodriguez, J. A., "Morphological effects of the nanostructured ceria support on the activity and stability of CuO/CeO_2 catalysts for the water-gas shift reaction," Phys. Chem. Chem. Phys. **16**, 17183–17195 (2014).

Zeng, S., Zhang, W., Sliwa, M., and Su, H., "Comparative study of CeO_2/CuO and CuO/CeO_2 catalysts on catalytic performance for preferential CO oxidation," Int. J. Hydrogen Energy **38**, 3597–3605 (2013).

Zhao, F., Li, S., Wu, X., Yue, R., Li, W., and Chen, Y., "Synergetic effect over flame-made manganese doped CuO–CeO_2 nanocatalyst for enhanced CO oxidation performance," RSC Adv. **9**, 2343–2352 (2019).